PERGAMON

International Journal of Heat and Mass Transfer 42 (1999) 3787–3802

International Journal of HEAT and MASS TRANSFER

www.elsevier.com/locate/ijhmt

The effect of streamwise vortices on the frost growth rate in developing laminar channel flows

B.D. Storey [1], A.M. Jacobi*

Department of Mechanical and Industrial Engineering, University of Illinois at Urbana-Champaign, 1206 W. Green Street, Urbana, IL 61801, USA

Received 4 September 1997; received in revised form 30 January 1999

Abstract

An experimental study is presented to assess the influence of streamwise vortices on frost growth in a steady, developing, laminar channel flow. Using a simple model and scale analysis, frost growth rate (ablimation) data are normalized with respect to temperature, humidity and time. Measurements from baseline experiments in a rectangular channel are found to be accurately correlated using the proposed scaling relation. Upon introducing streamwise vortices in the channel flow, frost growth still follows the scaling relation, but local growth rates were observed to increase by more than 7% in regions where the streamwise vortices induce a surface-normal flow toward the frost surface. Frost thickness measurements, flow visualization, and deposition patterns are used to explain these findings.

1. Introduction and background

1.1. Introduction

Finned heat exchangers are common in many refrigerant-to-air applications, and in these applications the air-side heat transfer often represents the largest thermal resistance and thus limits performance. One promising method to enhance air-side heat transfer is to use a vortex generator to induce streamwise vortices between the fins. The spiraling fluid motion is carried through the fin passage by the bulk flow, and the thermal boundary layer is effectively thinned, improving heat transfer. Various methods to generate such vortices have been studied and are reported in the literature [1,2]; example vortex generators and a schematic of the resulting flow are shown in Fig. 1. The use of streamwise vortices as a heat transfer enhancement scheme appears promising for plain fin-and-tube heat exchangers typical of those used in refrigerant-to-air applications.

In most refrigeration applications, frost forms on the fins because the surface temperature is below the freezing point of water and the dew point of the air stream. Frost has a deleterious effect on heat exchanger performance; it adds a thermal resistance and, through a blockage effect, reduces the air flow rate. Frost growth rate and properties are sensitive to temperature, humidity, fin surface characteristics, and air flow conditions. Thus, it may be anticipated that secondary flows—such as streamwise vortices—will affect frost growth.

Frost formation has been studied for many simplified configurations such as flow across cylinders and over flat plates; however, as far as is known, no studies of frost formation in developing internal flows with

* Corresponding author. Tel.: +1-217-333-4108; fax: +1-217-244-6534.

E-mail address: a-jacobi@uiuc.edu (A.M. Jacobi)

[1] Currently at University of California, Berkeley

0017-9310/99/$ - see front matter
PII: S0017-9310(99)00045-9

Nomenclature

b	span of delta-wing vortex generator (see Fig. 1) [m]
Bi	frost Biot number, hL_f/k_f (Eq. (9))
c	chord length of delta-wing (see Fig. 1) [m]
c_p	specific heat [kJ/kg K]
D_{ab}	binary diffusion coefficient for water in air [m^2/s]
D_h	hydraulic diameter, $2WH/(W+H)$ [m]
Fo	frost Fourier number, $\beta t/c_{pa}H^2$ (Eq. (7))
h	convective heat transfer coefficient [W/m^2 K]
H	channel height [m]
h_m	convective mass transfer coefficient [m/s]
Ja	Jakob number, $c_{pa}\Delta T_\infty/\lambda_{sg}$ (Eq. (7))
k	thermal conductivity [W/m K]
L_f	frost layer thickness [m]
Le	Lewis number, α/D_{ab}
m_f	water mass flux to frost surface [kg/s m^2]
Re	Reynolds number based on hydraulic diameter, VD_h/ν
t	time [s]
T	temperature [°C]
V	mean velocity of air flow in channel [m/s]
W	width of the channel (see Fig. 2) [m]
x	streamwise coordinate direction (see Fig. 2) [m]
y	coordinate direction normal to the plate (see Fig. 2) [m]
z	spanwise coordinate direction (see Fig. 2) [m]

Greek symbols

α	angle of attack of delta-wing [°], or thermal diffusivity [m^2/s]
β	change in frost conductivity with density, $\partial k_f/\partial\rho_f$, [W m^2/kg K]
Γ	non-dimensional frost thickness, L_f/H (Eq. (7))
ΔT_w	temperature change across frost layer (Eq. (4)) [°C]
ΔT_∞	temperature change, freestream to frost surface (Eq. (4)) [°C]
$\Delta\rho_v$	partial density change, freestream to frost surface (Eq. (4)) [kg/m^3]
Θ	temperature ratio, $\Delta T_\infty/\Delta T_w$ (Eq. (7))
Λ	aspect ratio of delta wing, $2b/c$ (see Fig. 1)
λ_{sg}	enthalpy of ablimation or sublimation of water [kJ/kg]
ν	kinematic viscosity [m^2/s]
ρ	density [kg/m^3]
τ	frost environmental time (Eq. (10))
Φ	dimensionless partial density change, $\Delta\rho_v/\rho_a$ (Eq. (7))

Subscripts

a	air
f	frost
fo	frost at time zero
g	gas phase in Woodside's equation
s	evaluated at frost surface, or solid phase in Woodside's equation
v	evaluated for water vapor, or with a vortex present
w	evaluated at cold wall
∞	free stream air

streamwise vortices have been reported. Understanding the impact of streamwise vortices on frost growth is important in assessing vortex generation as a practical heat-transfer enhancement method for refrigeration applications. Furthermore, because a horseshoe vortex system naturally forms at the fin–tube junction in fin-

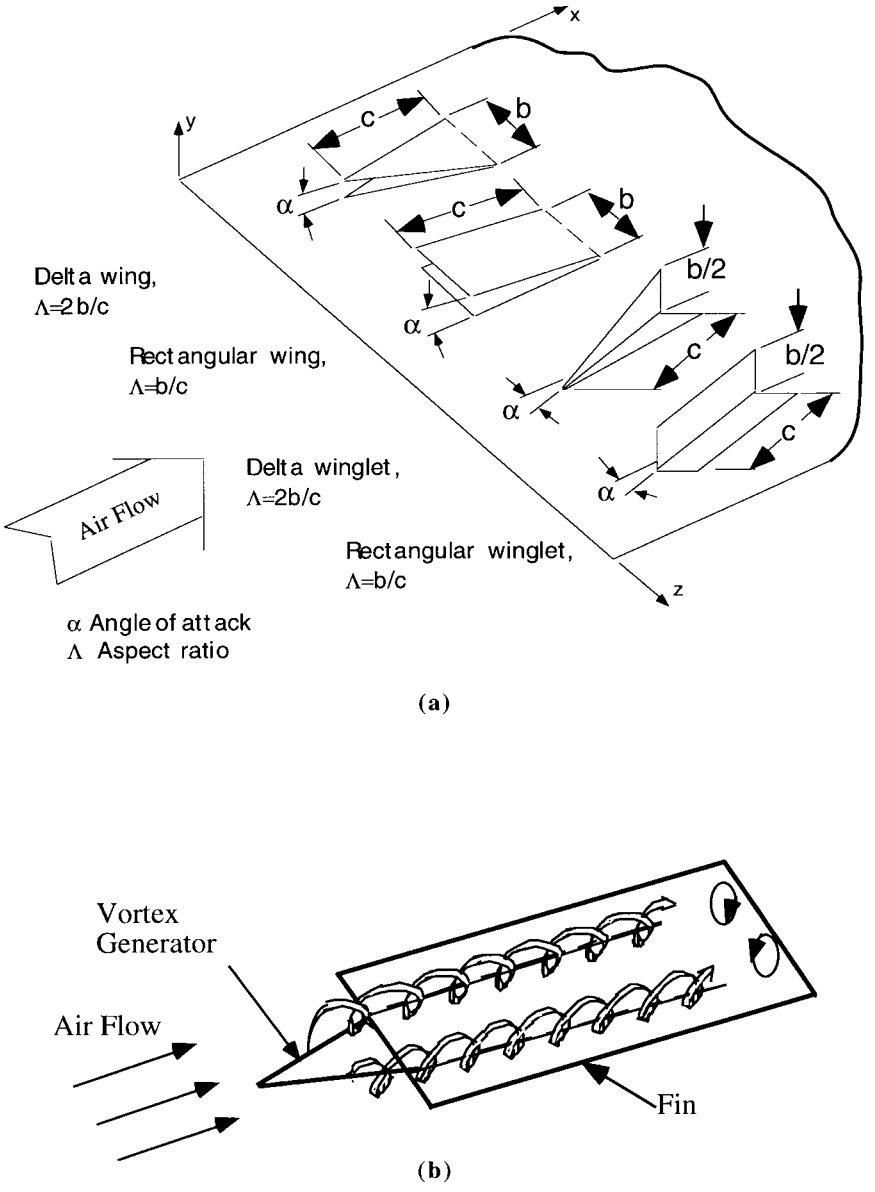

Fig. 1. Small-scale flow manipulators are used on heat transfer surfaces to generate streamwise vortices: (a) shows common vortex-generator geometries; (b) presents a schematic representation of the resulting flow. These figures are taken from Jacobi and Shah [1].

tube heat exchangers, understanding vortex–frost interactions may help in the design of conventional fin-tube evaporators for refrigeration applications. In this paper, the influence of streamwise vortices on the growth of frost in laminar channel flows is considered for conditions typical to refrigeration applications.

1.2. Background

Reviews of the literature have appeared describing many methods for generating and exploiting streamwise vortices for enhanced heat exchanger performance [1,2]. The current work will rely on delta wings located

on the channel floor to generate streamwise vortices. Because extensive reviews of vortex generation are available, only a survey of the literature related to delta-wing heat transfer enhancement is presented in this section to provide context for the current study.

In early work by Edwards and Alker [3] the effect of delta winglets and cubes on flat plate heat transfer was studied. They found that delta winglets provided a higher overall heat transfer enhancement, but cubes provided a higher local enhancement. A vortex pair that was co-rotating, i.e. with the same swirl direction, was less effective than counter-rotating vortices. Kataoka [4] conducted experiments showing that heat transfer was locally enhanced in the region where two neighboring vortices imposed a flow toward the surface; heat transfer locally decreased where vortices imposed a flow away from the surface. These results suggest that a surface-normal flow induced by the vortices causes boundary layer thinning, which in turn enhances heat transfer.

Fiebig and co-workers [5] conducted an experimental comparison of delta wings, delta winglets, rectangular wings, and rectangular winglets[2]. The heat-transfer enhancement relative to a plain-channel baseline was found to be independent of Reynolds number and to increase with wing angle of attack. Overall enhancements reached 60% higher than the baseline channel flow. Delta wings and winglets were found to be more effective for heat transfer enhancement than rectangular wings and winglets. This work was extended [6] to study single and double rows of delta winglets in channel flows. Local heat-transfer enhancements several times the baseline channel-flow results were reported, suggesting this method as a promising approach to enhanced heat exchanger performance.

Biswas and Chattopadhyay [7] considered the influence of Reynolds number and angle of attack on skin friction and heat transfer. In this computational study, the effect of a stamped hole underneath the wing was considered; such a hole results when fin material is used to form the wing (see Fig. 1). Their computations indicated that vortex circulation is reduced when a hole is present under the wing because fluid flows into the adjacent channel rather than rolling up around the wing. Higher enhancements in overall heat transfer were predicted for the case without stamping.

For the simple case of a flat plate with a delta wing attached to its leading edge, Gentry and Jacobi [8] presented a method for selecting the preferred wing aspect ratio and attack angle. A single parameter, a *goodness factor*, was developed based on the idea that a high circulation vortex placed near the edge of the thermal boundary layer was preferred. The goodness factor was calculated from flow visualization data, and its utility in guiding vortex generator design was demonstrated through experiments. A similar approach might be useful in applying vortex enhancement to heat exchangers.

Considerable research has been conducted on using streamwise vortices to enhance heat exchanger performance. Unfortunately, no work on using this method under the frosting conditions typical to refrigeration applications is available. Although no reports on frost growth in a laminar channel flow with streamwise vortices were found in the open literature, a number of germane studies of frost growth were identified, and they are surveyed below to provide context for the current study.

In early frost formation work, Coles [9] experimentally studied the thermal conductivity of frost formation on aircraft wings. Under these conditions, the frost thermal conductivity was well correlated with density and agreed with data for packed snow. Yonko and Sepsy [10] conducted experiments to measure frost thermal conductivity for the conditions found in refrigeration applications. The results indicated that thermal conductivity strongly depended on density, but that other factors could be important. Yonko and Sepsy found frost layer thickness to be independent of Reynolds number.

Brian et al. [11] compared experimental results for frost formation between parallel plates to a mathematical model developed in their earlier work [12]. The model predicts that water vapor diffuses from the frost surface to the colder interior—that is, from the frost–air interface into the layer. This diffusion is driven by a gradient in the partial pressure of water caused by the temperature distribution in the frost layer. No quantitative comparison of the data to the model was provided, nor was generality of the model tested over a range of environmental conditions.

Biguria and Wenzel [13] measured the thermal conductivity of frost forming on a flat plate for a variety of environmental conditions. These experiments showed the frost thickness to decrease and thermal conductivity to increase with increasing air velocity. The frost thickness was found to be constant and the thermal conductivity to decrease with distance down the plate. Biguria and Wenzel explained their observations of frost growth in terms of a critical cluster mechanism.

Yamakawa et al. [14] measured heat and mass transfer coefficients over a frost layer in channel flow for a wide range of environmental conditions. Temperature measurements of the thermal boundary layer showed a thinner layer for the case of higher mass flux to the frost surface, indicating an increase in heat transfer with mass flux. In exploring the relationship between

[2] A wing is attached to the fin along its base and a winglet along its chord (see Fig. 1).

heat and mass transfer, the heat transfer coefficients were higher than expected through the heat-mass analogy. Yamakawa and co-workers found the deviation was beyond that attributable to a simple boundary-layer suction effect.

Hayashi et al. [15] conducted an experimental study to classify the stages and formation types occurring in frost growth. They divided the growth into three periods: crystal growth, frost layer growth, and a full-growth frost layer. The crystal growth period is characterized by one-dimensional growth of ice crystal columns normal to the wall. In the frost layer growth period, the frost becomes more homogeneous and continues to grow in thickness as the crystals begin to branch together. The full-growth period begins when the surface of the frost reaches the melting point and the frost grows in a continuous cycle of melting and re-freezing. A structural model of the layer was developed to predict the thermal conductivity of the frost layer using Woodside's equation[3] [16].

Schneider's [17] experiments on frost growth on a cylinder in cross flow showed growth rate to be independent of Reynolds number and location on the cylinder. He presented a model based on the assumption that nucleation depends on Reynolds number and arrangement of the test surface, but growth rate is dependent on the supersaturation ratio and frost conductivity. A model of heat transfer in a single needle of ice, adjusted with empirical results, provided an equation to predict frost deposition thickness as a function of environmental parameters and time. Schneider's equation predicted his experimental data and data from other studies to within 10%.

Tao et al. [18] developed a mathematical model of the frost layer growth stage by treating the frost as a porous medium with distributed porosity. The model predictions showed a spatial variation of frost density consistent with that found experimentally by other investigators [19]. The model was compared to experimental data by Mao et al. [20] and predicted the general trends for the limited comparisons given.

Sahin [21] presented a theoretical model of the crystal growth period. A simple model was proposed assuming that cylindrical frost columns grew in height and radius with time. The model required an initial value of the ratio of frost column area to total surface area. Sahin determined a value of this area ratio such that his model predicted the experimental results from earlier work [22] with a minimization in error. Sahin did not compare the area ratio found in this manner to data from experiments, nor did he discuss what values were physically reasonable.

The literature survey reveals considerable research directed toward characterizing the heat transfer enhancement through vortex generation in plain fin-and-tube heat exchangers. Likewise, there has been considerable research on frost growth in simple flows. Unfortunately, there has been no research on frost growth in developing channel flows with streamwise vortices. Understanding the interaction between streamwise vortices and frost growth is important in assessing the potential of vortex generation in refrigeration applications; furthermore, it may guide conventional designs where a horseshoe vortex system naturally occurs. In this paper, a non-intrusive, laser imaging method is used to accurately measure frost thickness. A scale analysis is used to clarify environmental, spatial, and temporal effects and to guide data interpretation. Data are presented to characterize frost growth in laminar channel flows with and without a vortex generator, and the mechanisms through which streamwise vortices affect the deposition and structure of frost are explored. Finally, the results of this research are discussed with respect to refrigerant-to-air heat exchanger applications.

2. Methods

2.1. Experimental setup

The experiments were conducted in a small test channel connected to a large closed-loop wind tunnel. The large tunnel[4] was used to provide air to the test channel with the desired temperature, humidity, and flow rate. Flow entered the test channel by passing through a set of screens, a honeycomb, and a 4-to-1 area contraction, as shown in Fig. 2. Downstream of the contraction, the cross-sectional area was 12.7 by 50.8 mm, and the flow passed through a development channel with a length of 632 mm (31 hydraulic diameters) before entering the test section where measurements were obtained. The test section is described below in detail. The air temperature at the test-section inlet was measured using a grid of five thermocouples

[3] Woodside's original paper contains a typographical error that has been duplicated in the literature. The correct *Woodside's equation* is

$$k = k_g\left(1-\left(\frac{6(\rho-\rho_g)}{\pi(\rho_s-\rho_g)}\right)^{1/3}\left(1-\frac{a^2-1}{2a}\ln\left(\frac{a+1}{a-1}\right)\right)\right)^{-1}$$

where

$$a = \sqrt{1+\frac{4}{\pi}\left(\frac{k_s}{k_g}-1\right)^{-1}\left(\frac{6(\rho-\rho_g)}{\pi(\rho_s-\rho_g)}\right)^{-2/3}}$$

[4] This large wind tunnel and its thermal conditioning equipment have been described in detail by Davis [23].

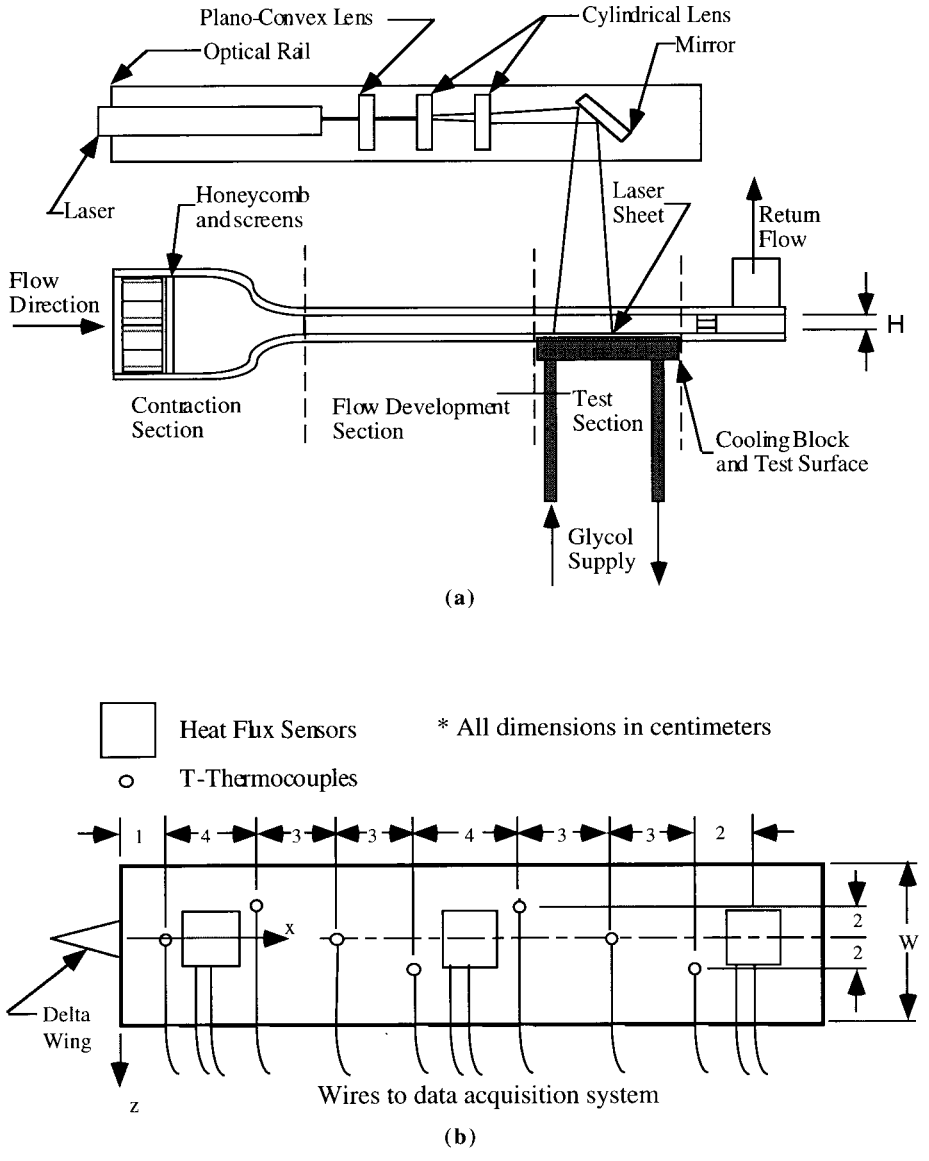

Fig. 2. This test section was supplied conditioned air at a controlled flow rate, temperature, and humidity. The rectangular flow cross section in test section had a height of $H = 12.7$ mm, and a width of $W = 50.8$ mm. The test section was 260 mm long and was preceded by a development section 632 mm long: (a) an overall schematic of the test channel; and (b) location of instruments and the vortex generator on the frost test surface (channel floor).

and the humidity was measured using a capacitance-film sensor. The air flow rate was measured using an ASME standard orifice plate located in the return pipe to the large wind tunnel.

The test section was 12.7 mm high, 50.8 mm wide, and 260 mm long. The bottom of the test section was chilled, and frost grew on the channel floor. The channel sides were made of acrylic and were insulated during experiments. The removable channel top was made of clear acrylic, allowing visual access and easy cleaning of the test surface. The test surface was mounted on an assembly consisting of an aluminum block with coolant passages and a 3.2-mm thick copper plate bolted to the chilled block to provide surface-temperature uniformity. Ethylene glycol was used to chill the aluminum block. Seven thermocouples and three heat flux sensors were mounted flush with the upper surface of the copper plate, and the aluminum test surface was clamped to it—aluminum is a typical heat exchanger fin material. All metal–metal interfaces

were coated with a thermally conductive paste to reduce contact resistance. The temperature drop across the thin aluminum test surface was estimated to be much smaller than the instrument uncertainty. The measured surface temperature distribution in the spanwise direction was uniform to within the instrument uncertainty, and variations in the streamwise direction were less than 0.5°C for all experimental conditions to be reported later in the paper.

The frost thickness was measured with a laser-sheet imaging technique. A 15 mW helium–neon laser beam was focused and spread into a sheet using a pair of cylindrical lenses. The sheet was directed at the test surface and a CCD camera recorded the reflection of the laser sheet. This laser imaging system also provided flow visualization if smoke was introduced upstream of the test section.

The instruments were connected to a data acquisition system, and 20 readings from each instrument were sampled and averaged (a period of approximately 30 s). These averages were logged and later processed to determine the environmental conditions of the test. Frost surface images were acquired at regular intervals depending on the desired length of the test. Storey [24] provides a more detailed description of the experimental apparatus.

2.2. Measurement uncertainty and experimental procedure

The laser and optics were arranged to provide the desired laser sheet size, orientation, and location for each test, and the camera was fixed and focused to provide the desired field of view. Once the optical system was in place, several images of a calibration block were recorded—the calibration block was a machined aluminum block with steps of known height. The calibration images were analyzed using intensity profile plots showing pixel intensity averaged over a window width and plotted against location along a line perpendicular to the calibration surface. By selecting the surface location to correspond to the maximum average pixel intensity, image-scaling factors were determined for each setup prior to an experiment. The calibration uncertainty (i.e. precision error) depended on camera location, laser-sheet focusing and position, with a typical 2-σ precision error of ± 50 μm in thickness (y), and ± 200 μm in location (x, z). A variation of this technique was used to characterize the frost surface profiles due to the streamwise vortices. Rather than averaging over a set of image windows, a high-order polynomial was fit to the thickness data using a least-squared error approach. This slight variation in the method served to locally smooth the data and was found to be superior to other methods such as changing the profile plot window size.

Table 1
Range and uncertainty of controlled environmental variables

Variable	Range	Uncertainty
T_∞	~20°C	±0.2°C
T_w	−23–−6°C	±0.2°C
RH	30–70%	±2%RH
Re	300–2500	±2.5%
x	3–13 cm	±0.2 mm
t	0–2.5 h	±1 min

The final uncertainty in frost thickness determined with the laser-imaging system depended on each optical setup and the nature of the frost. The surface was difficult to analyze early in the crystal growth period because the crystal-like structures caused a poor reflection of the incident laser sheet. During early crystal growth, the uncertainty in frost thickness measurement was estimated to be as high as ±300 μm, during the mature growth phase, the average uncertainty was between ±200 μm and ±100 μm, depending on the test conditions and time (see ref. [24] for details).

Each test was initiated by setting the wind tunnel inlet air temperature, humidity, and velocity. The ethylene-glycol chiller system was set to the desired temperature and was allowed to bypass the test surface until the start of a test. The test surface was cleaned with a soft cloth and alcohol before each experiment. A test began by opening the valve to allow coolant flow to the test surface. The experimental range and uncertainties in measured conditions are given in Table 1. In some experiments, variations in the test conditions occurred during the experiment, and sometimes these variations were beyond the experimental uncertainties. For all experiments to be reported, the average 2-σ variation in test conditions was less than 0.3°C for air temperature, 1.0°C surface temperature, and 2.2% for the inlet relative humidity. During the experiments the air flow rate was altered by the frost growth through its affect on hydraulic diameter. The maximum change in *Re* due to this effect was 8% and, as discussed later, the results were unaffected by changes in *Re*.

2.3. Data interpretation

Because frost thickness is sensitive to environmental conditions, it is important to normalize these effects when comparing different flow situations. An appropriate normalization is suggested by a scale analysis using the following model equations for frost growth:

$$k_f \frac{dT}{dy}\Big|_{y=L_f} = h(T_\infty - T_s) + \lambda_{sg} m_f \quad (1)$$

$$m_f = \frac{d}{dt}\int_0^{L_f} \rho_f \, dy \tag{2}$$

and

$$m_f = h_m(\rho_{v,\infty} - \rho_{v,s}). \tag{3}$$

Eq. (1) is based on heat flux continuity at the frost–air interface. Eq. (2) is an expression for the conservation of water in the frost layer, and Eq. (3) is the convective rate equation for mass transfer in a dilute solution.

Data provided by Hayashi and co-workers [15] show that frost thermal conductivity can be plotted as a family of curves: the variation of the thermal conductivity with density is nearly the same for all conditions but the value of the conductivity depends on the environment. Thus, to a first approximation $k_f = k_{fo} + \beta\rho_f$, where the intercept, k_{fo}, is dependent on the environment but the slope, β, is constant for a wide range of conditions. This simple model breaks down at very low and high frost densities. Furthermore, except very early in time (i.e. except for very thin layers) $\beta\rho_f \gg k_{fo}$.

Using Eqs. (1)–(3), and assuming $k_f \sim \beta\rho_f$ the frost layer is found to obey the following scaling relation:

$$h_m \Delta\rho_v \frac{\beta t}{L_f}\frac{\Delta T_w}{L_f} \sim h\Delta T_\infty + \lambda_{sg} h_m \Delta\rho_v \tag{4}$$

where

$$\Delta T_w = T_s - T_w, \quad \Delta T_\infty = T_\infty - T_s$$

and $\Delta\rho_v = \rho_{v,\infty} - \rho_{v,s}$.

Because which term will dominate the right-hand side of Eq. (4) depends on environmental conditions and cannot be determined a priori, both terms are retained (in the form of a sum). The convective heat and mass transfer coefficients can be related through the heat and mass analogy:

$$h = h_m \rho_a c_{pa} Le^{1-n} \tag{5}$$

where the Lewis number is $Le = \alpha_a/D_{ab}$, and the power $1 - n = 2/3$ will be adopted. Using Eq. (5) in Eq. (4) and rearranging yields the scaling relation

$$\frac{\beta t}{c_{pa} L_f^2} \sim \frac{\Delta T_\infty}{\Delta T_w}\left(\frac{\rho_a Le^{2/3}}{\Delta\rho_v} + \frac{\lambda_{sg}}{c_{pa}\Delta T_\infty}\right). \tag{6}$$

Eq. (6) can be expressed as an equality if β is simply regarded as a scaling constant:

$$\frac{Fo}{\Gamma^2} = \Theta\left(\frac{Le^{2/3}}{\Phi} + \frac{1}{Ja}\right) \tag{7}$$

where

$$Fo = \frac{\beta t}{c_{pa} H^2}, \quad \Gamma = \frac{L_f}{H}, \quad Ja = \frac{c_{pa}\Delta T_\infty}{\lambda_{sg}}, \quad \Theta = \frac{\Delta T_\infty}{\Delta T_w},$$

and $\Phi = \dfrac{\Delta\rho_v}{\rho_a}$.

In Eq. (7), β is considered as an unknown constant to be determined from experimental data. Using the definitions provided above, an expression for β can be developed in dimensional form to make its experimental assessment more straightforward

$$\beta = \frac{c_{pa} L_f^2 \Delta T_\infty}{t\Delta T_w}\left(\frac{Le^{2/3}\rho_a}{\Delta\rho_v} + \frac{\lambda_{sg}}{c_{pa}\Delta T_\infty}\right). \tag{8}$$

With β determined from experiments using Eq. (8), the relationship between frost thickness, environmental conditions, and time is expressed through Eq. (7). However, it is convenient to re-write this expression using the frost Biot number. The conventional form of the Biot number can be obtained by rearranging Eq. (1). The Biot number can then be written as a function of the environmentally dependent dimensionless parameters.

$$Bi = \frac{hL_f}{k_f} = \frac{Ja\, Le^{2/3}}{\Theta(Ja\, Le^{2/3} + \Phi)} \tag{9}$$

The Biot number represents the relative magnitudes of heat transfer resistance due to conduction through the frost layer to the convection resistance at the frost surface. Finally, using the definition of the Biot number, Eq. (7) becomes

$$\Gamma = \sqrt{\tau} \tag{10a}$$

where the frost *environmental time*, τ, is defined as:

$$\tau = \frac{Fo\, Bi\, \Phi}{Le^{2/3}} \tag{10b}$$

Eq. (10) concisely shows the effect of environmental conditions on frost growth. It should be noted that using the channel height as a length scale (Eq. (7)) is somewhat arbitrary. The channel height does not directly affect the growth rate of the frost, nor is the channel height physically relevant to the frost growth equations. The channel height was selected so that $\Gamma = 1$ when frost has bridged the channel. For the present case this length scale offers the added convenience that it can be used to calculate pressure drop associated with the airflow through the frosted passage; thus, the frost growth and channel flow can be coupled (ref. [24] gives such an analysis.).

The frost surface temperature must be known in order to evaluate the environmental time, but in the current study such measurements of frost surface temperatures were not obtained. Published data show that

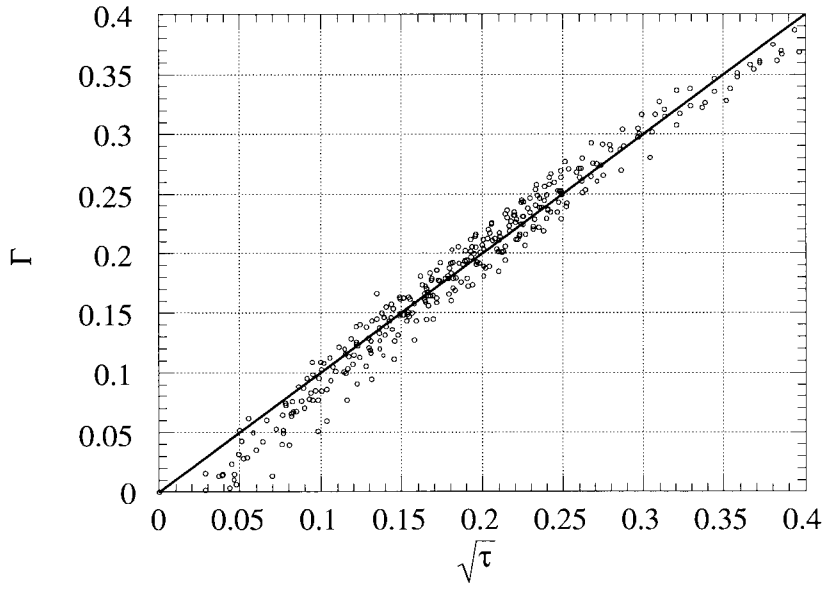

Fig. 3. Dimensionless thickness data are shown for laminar channel flows over the conditions given in Table l. No vortex generator was used in these experiments. The solid line represents the scaling relation of Eq. (10), and the collapse of the data indicates that a proper scaling has been achieved.

frost surface temperature tends to the freezing point as time progresses. Therefore, Eq. (10b) is evaluated with T_s taken as the freezing point. Taking T_s as constant is equivalent to assuming a constant mass flux to the frost layer for fixed environmental conditions (cf. Eq. (3)). Such an assumption is supported by observations over a range of thermal and flow conditions [14,20,25]; however, it is certainly untenable very early in time, i.e. as $t \to 0$. Likewise, the model for frost thermal conductivity put forward by Hayashi and co-workers breaks down at early times. Therefore, Eq. (10) may be expected to fail at early times. Finally, it should be noted that the exact form of the heat and mass analogy may change for other flow situations and care should be used in extending this model beyond the current experimental conditions. The simplifications notwithstanding, Eq. (10) captures the essential physics of mature frost growth and will be demonstrated as a useful tool for data interpretation.

3. Results and discussion

3.1. Results

In order to evaluate the effects of a vortex generator on frost growth rate and frost properties, baseline experiments over a wide range of environmental conditions for flow in a plain channel were conducted. The experimental range and measurement uncertainties are summarized in Table 1; these conditions correspond to the following range in the non-dimensional parameters defined earlier: $Ja \sim 7.1 \times 10^{-3}$; $Le \sim 0.91$; $0.87 < \Theta < 3.3$; $2.7 \times 10^{-4} < \Phi < 5.8 \times 10^{-3}$; and $0 < Fo < 40$. These plain-channel frost growth data add to the current literature since few data have been reported for these conditions. Most of the data in these tests were collected for Reynolds numbers below 1200.

Using 291 observations from the baseline channel flow case and Eq. (8), the mean value of β over the entire experimental range was found to be 8.7×10^{-4} W/m^2/kg K with an RMS deviation less than 13%. Because Eq. (10) may break down at very early times, data with $\sqrt{\tau}<0.1$ were not used in calculating β.

The dimensionless frost thickness for the baseline channel flow, Γ, is plotted against the square root of the frost environmental time, $\sqrt{\tau}$, in Fig. 3. The uncertainties in Γ and $\sqrt{\tau}$ depend on the specific operating conditions and testing times. Using standard error-propagation methods and the uncertainties in Table 1, the typical 2-σ uncertainty for $\sqrt{\tau}$ under mature-growth conditions was 8% while the uncertainty for Γ was 3% to 6%; uncertainties in both variables increase at early times. Eq. (10), developed through the scale analysis, successfully collapses the data to within the uncertainty of the measurements. The initiation of frost growth ($\tau = 0$) was determined by noting a spike in the measured heat flux associated with the release of latent heat of fusion. The early-time deviation of the data from the predicted behavior probably reflects a

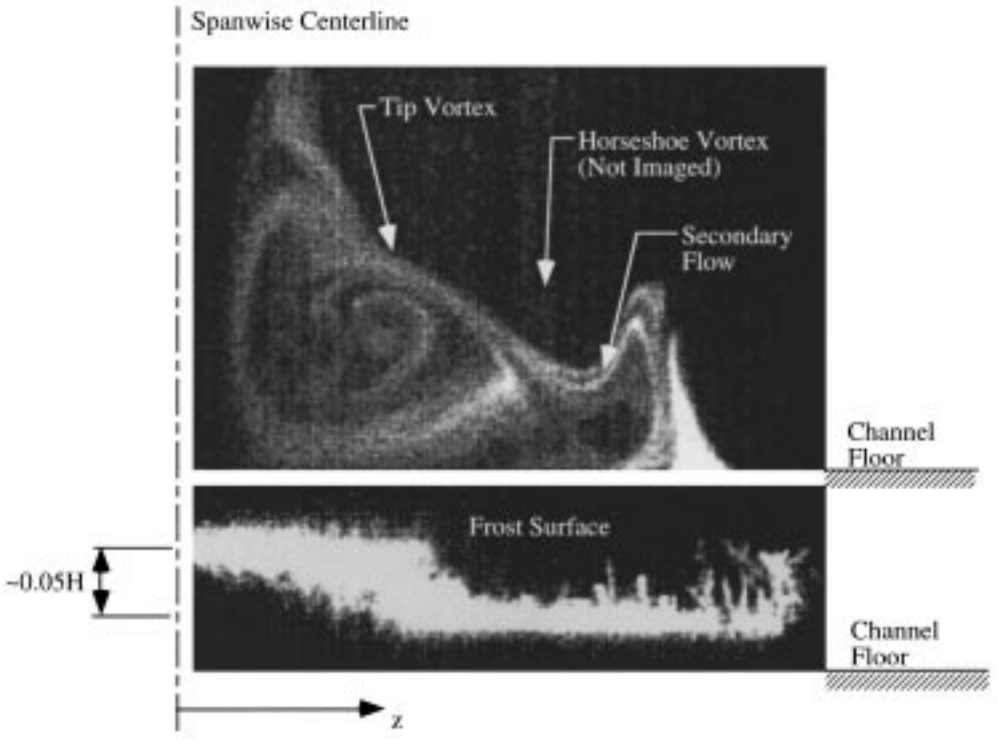

Fig. 4. An example of flow and frost structure. In the upper image, smoke was used to mark the developing channel flow downstream from a delta wing attached to the channel floor ($b=7.5$ mm, $\Lambda=1$, and $\alpha=40^\circ$). The camera remained in place, and frost was allowed to grow. The lower image was recorded by photographing the frost surface reflection of the laser sheet. Quantitative results over a range of operating conditions are presented in the figures that follow.

breakdown of the scaling embodied in Eq. (10) for $\sqrt{\tau}<0.1$. This breakdown could be caused by temporal variations in frost surface temperature (or mass flux) during the crystal growth period. However, it should be noted that data interpretation is made more difficult by the higher uncertainty in measured frost thickness at earlier times. In spite of difficulties in measuring, understanding, and predicting the very early-time data, the baseline results clearly demonstrate a proper normalization through Eq. (10). Experiments directed toward understanding the impact of streamwise vortices will be interpreted using this approach.

For this study, streamwise vortices were generated using a single delta wing fixed to the lower surface of the channel and centered in the spanwise direction as shown in Fig. 2. The wing generated a common-inflow, counter-rotating pair of tip vortices, causing a local enhancement in the heat and mass transfer coefficients. Because the wing was placed on the solid channel floor, a horseshoe vortex system formed around the base of the delta wing. For the results to be presented, the wing geometry was: $b=7.5$ mm, $\Lambda=1$, and $\alpha=40^\circ$; experiments with other wings gave qualitatively similar results [24].

The flow field was investigated to help understand the relationship between the local flow conditions and local frost growth rate and structure. The flow field was visualized using the same laser imaging method used in thickness measurement, but smoke was injected into the flow at an upstream location. Frost thickness data were not collected during the visualization experiments because it was unclear how the smoke might affect frost growth. One side of the symmetric vortex flow and the corresponding frost growth at the same location is shown in Fig. 4 (a 'snapshot' in time). The frost had a more homogeneous structure in the region corresponding to the downwash and transverse velocity regions of the tip vortex. The flow structure imaged on the right side of the figure is a secondary flow caused by the main horseshoe vortex. Note that the main horseshoe vortex was not imaged in this figure—it was located above the induced secondary flow and is shown clearly in later figures. The frost deposition changed markedly when the vortex-induced flow began to turn away from the frost surface. In Fig. 4, little frost growth had occurred in this upwash region. At the extreme right side of the image, where the effects of the vortices were not felt, frost grew at a rate simi-

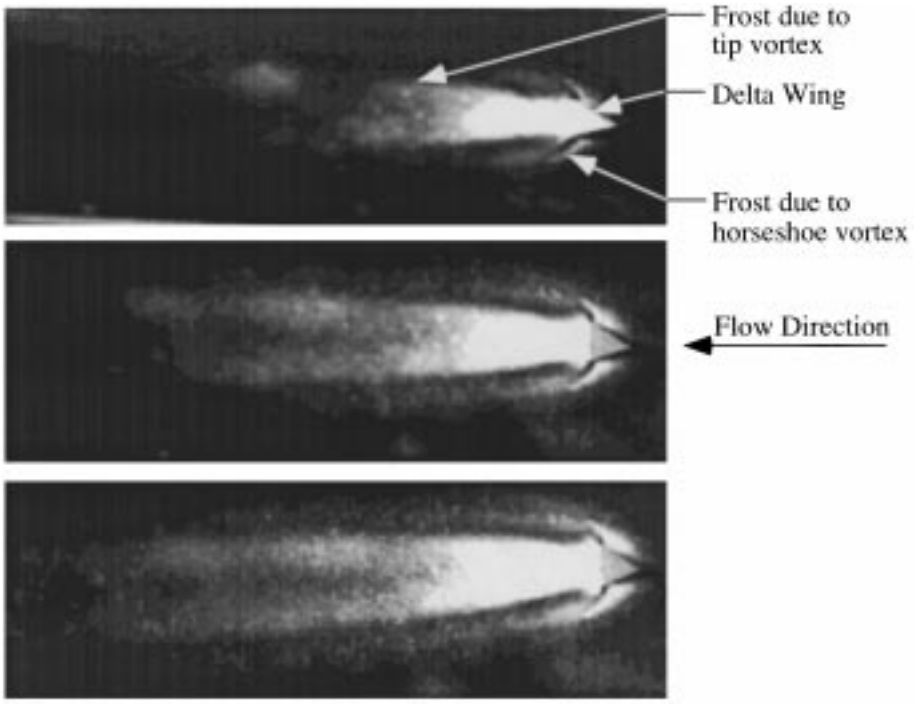

Fig. 5. Photographs of frost deposition patterns behind the delta wing at $Re = 1030$. The top image shows frost at approximately 130 s, the middle at 280 s, and the bottom image at 490 s. The flow length (in x) is about 150 mm for each image.

lar to the region under the vortex. The frost in this outer region was still in the crystal growth stage while the frost under the vortex had a solid and homogeneous structure. Although the frost structure was different, the height of the crystals in the outer region was approximately equal to the height under the tip vortex.

Photographs of early frost deposition patterns behind the delta wing at different times are shown in Fig. 5. For these photographs, the channel surface was painted black to provide good visual contrast between frosted and unfrosted locations. The paint did not affect the qualitative results and was not used during the quantitative thickness measurements. Frost inception first occurred directly behind the wing and followed the path of the two tip vortices as they were advected down the plate. The horseshoe vortex system caused the streaks of frost that wrap around the wing and sweep downstream. The interaction between the tip and horseshoe vortices as they are carried down the channel is detailed in Fig. 6. The tip vortex is the larger vortex on the left side of each image and the horseshoe vortex is on the right. The flow visualization results show that the flow induced by the tip vortex carries the horseshoe vortex away from the frost surface and into the channel flow. As the two vortices were advected down the plate, the horseshoe vortex was distorted and apparently merged with the tip vortex. The impact of this interaction is reflected by the frost deposition results. As the horseshoe vortex is carried downstream and away from the frost surface, its effect on frost deposition is diminished as shown schematically in Fig. 6 (see also the photographs of Fig. 5).

Interactions between the flow field and frost growth changed as a frost layer grew on the channel floor. The frost thickness variations in the spanwise direction at different times are shown in Fig. 7 for a particular environment. At early times, little variation in frost thickness with spanwise location was observed (the differences can be explained by small differences in nucleation time). As time progressed, the frost grew faster where the vortices induced a surface-normal flow toward the frost layer, and there was a slight decrease in growth rate associated with the surface-normal flow away from the frost layer. In regions far away from the vortices, the growth rate was equal to that observed in the baseline channel flow experiments. The location of maximum frost thickness shifted toward the centerline as time progressed. This effect was caused by the decrease in exposed wing area as the frost grew around the wing. The variations in frost thickness on the right side of the figure seen at early times were caused by the horseshoe vortex.

In order to evaluate the impact of streamwise vortices on frost deposition over an extended period of

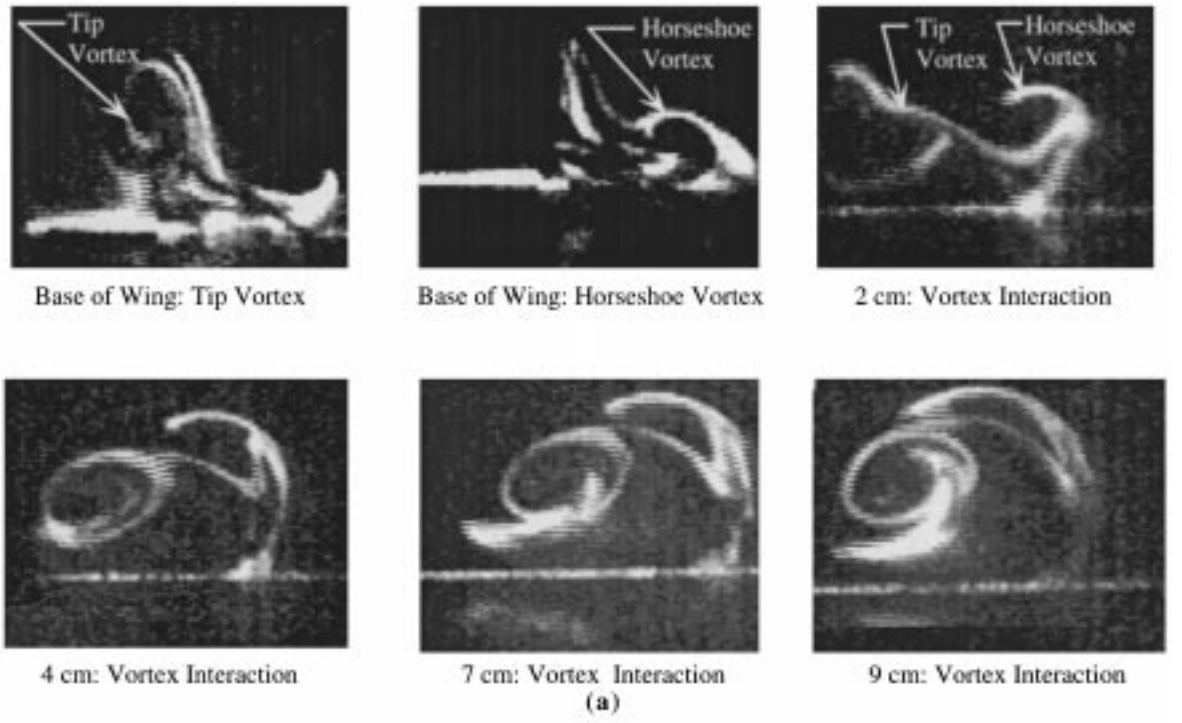

Fig. 6. Interactions between the horseshoe and tip vortices: (a) laser-sheet illuminated smoke images are shown at streamwise (x) locations from the delta-wing base to $x=90$ mm at $Re=330$; (b) a cartoon showing how the tip vortex lifts the horseshoe vortex into the channel flow; eventually the two streamwise vortices merge.

growth, a series of experiments were conducted for a range of conditions similar to those used to obtain the plain-channel data. Using the value of β determined from the plain-channel data, Fig. 8 shows the maximum frost thickness plotted against the square root of the frost environmental time. Contrasting the data shown Fig. 8 with the plain channel results, the maximum frost thickness behind the delta-wing is larger than in the plain-channel case. Using the data reported in Fig. 8 for the vortex-enhanced flow (137 points), a value of $\beta_v=1.0\times10^{-3}$ W m^2/kg K was determined. This value is 15% higher than that found in the plain-channel flow and represents an increase frost growth rate over the baseline channel flow of 7.2%.

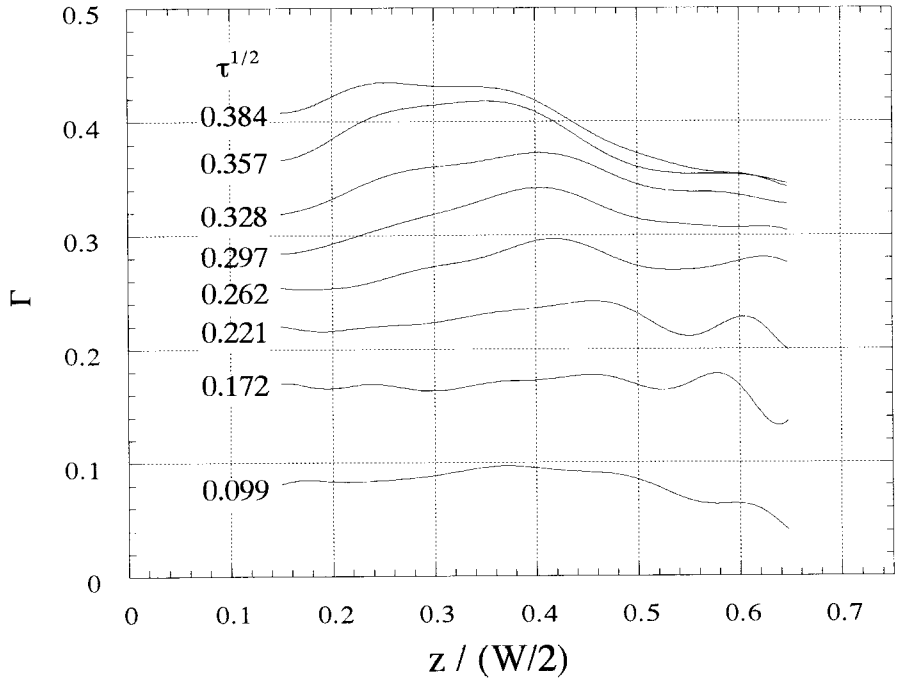

Fig. 7. Spanwise profiles of frost thickness at a fixed streamwise location over increments of 1000 s from the start of the test (not from frost inception). Note that the growth rate changes after initially being nearly constant over the entire span. Also note that the location of maximum frost thickness moves toward the centerline with time due to the decreased size of the delta wing as frost grows around the wing. The test conditions were as follows: $Bi = 0.586$, $\Phi = 5.84 \times 10^{-3}$, $Re = 1000$, and $x = 13$ cm.

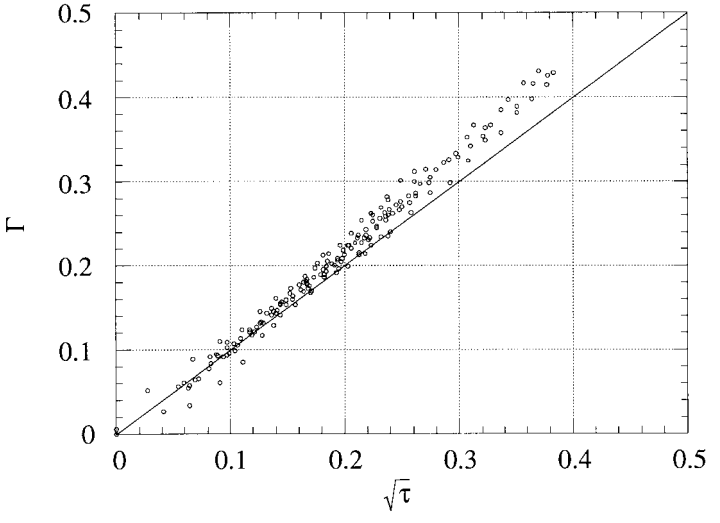

Fig. 8. Dimensionless thicknesses at the spanwise location where it is a maximum for frost growth downstream from the delta-wing vortex generator. The experimental conditions span those given in Table 1, and the plot is constructed using the value of β determined from the baseline case (with no vortex generator). The data collapse in Γ–$\sqrt{\tau}$ space; however, they reflect a growth rate 7.2% larger than in the baseline case.

3.2. Discussion

The scale analysis shows that the influence of heat transfer coefficient on frost growth cancels out through the heat and mass transfer analogy. The success of this approach in modeling the experimental data strongly suggests that frost growth in a channel flow is insensitive to Reynolds number and spatial variations in the heat transfer coefficient. The scale analysis also shows that frost growth is proportional to the square root of time (see Eq. 10); this behavior has been observed in mature frost growth by many investigators. A frost thickness proportional to the square root of time was also found by Georgiadis [26] in the crystal growth period and by others studying the growth of ice crystals in clouds [27]. If m_f is assumed constant, Eq. 2 can be used with the data to show that average frost density increases with the square root of time.

Eq. (10) can be rearranged into a form similar to the equation developed by Schneider [17]. Schneider's equation was based on different physical arguments but predicted identical effects of time and plate temperature on frost thickness—Schneider predicted a different dependence on humidity and air temperature. Using Eq. (10) and the value of β obtained for the baseline channel-flow experiments, the data reported by Schneider were predicted by the current model to within the experimental uncertainty. Likewise, the conditions reported by Mao [28] were considered, and although Mao's data were recorded at higher Reynolds numbers (3000–7000) most of those data were predicted to within the experimental uncertainty. Eq. (10) showed a slight bias toward under predicting the frost thickness measured by Mao, probably due to the higher Reynolds numbers at which those data were obtained.

The qualitative results from flow visualization are useful in understanding the complex interactions between the flow and the frost growth—how vortices affect frost deposition. A few additional observations from these studies are noteworthy. Increasing the Reynolds number caused both the horseshoe and tip vortices to spread further from the centerline due to the increase in the vortex circulation and interaction of the vortices with the channel floor (for a detailed discussion of this behavior, see ref. [29]). With an increasing Reynolds number, the horseshoe vortex system was influenced less by the tip vortices; this observation was consistent with the frost deposition photographs: the streaks of frost deposition due to the horseshoe vortex became more pronounced with an increase in Reynolds number. If the Reynolds number was too high, the horseshoe vortex broke down and the deposition patterns around the wing became less defined. The tip vortex also broke down as the Reynolds number was increased—this breakdown occurred near $Re = 1200$. The exact conditions that caused vortex breakdown were not investigated, but related results have been reported [2].

Both Figs. 7 and 8 indicate an increase in frost growth due to streamwise vortices. In Fig. 7, the frost thickness profile showed little dependence on spanwise location for some initial period, then at later times frost growth in the downwash region of the vortex was slightly faster than in regions unaffected by the vortex flow. The results in Fig. 8 are consistent, with little deviation from the plain-channel results at early times but an increased thickness at later times. While the coupling between the vortex flow and frost growth is clear from these data, the physical mechanism remains somewhat unclear. Faster frost growth may be due to deviations from the assumed heat and mass transfer analogy. If the actual h–h_m relation deviated in the manner suggested by Yamakawa's data [14], then an increased growth rate could result. Supporting this conjecture, Mao's data for turbulent channel flow, where a different form of the heat and mass analogy prevails, also reflect growth rates slightly higher than the laminar plain-channel scaling suggests. Another possibility is that the vortex-induced velocity causes spatial variations in frost density and conductivity—effects unaccounted for in the current model. Given that variations in local heat transfer coefficient of several hundred percent have been reported for delta-wing vortex generation [1], it is remarkable that the effect on frost thickness is limited to about a 7% deviation from the plain-channel case.

Delta-wing vortex generators have been reported to provide local heat transfer enhancements of several hundred percent through the effects of streamwise vortices in a channel flow. The current research showed such vortices to produce a 7.2% increase in maximum frost thickness. Assuming an analogy between heat and mass transfer, the overall impact of the vortex generator under frosting conditions is to locally deposit more frost mass in only a slightly thicker frost layer, creating a denser frost layer. Therefore, vortex generators simultaneously increase the local heat transfer coefficient and decrease the thermal resistance of the frost, providing an overall improvement in heat transfer performance. The additional pressure drop in the channel due to the effect of the vortex on the frost is minimal since the frost thickness is not significantly increased. The pressure drop due to the delta-wing itself was not evaluated in this work but has been studied by others [1,2,29]. Therefore, the use of vortex generators to enhance refrigerant-to-air heat exchanger performance under frosting conditions appears promising. Future evaluations should be conducted for full-scale heat exchangers to properly evaluate the heat transfer and pressure drop in the complex flows of application.

4. Conclusion

Frost formation is complex, and frost layer thickness is sensitive to environmental parameters and growth history. A scale analysis of simplified model equations was used to guide data interpretation and correlation for frost growth in a laminar channel flow with and without vortex generators. The scale analysis yielded the simple model of frost growth given in Eq. (10). Although more complete models of frost growth have been presented in the literature [12,18,21], these models require information on convective heat transfer coefficient, frost thermal conductivity, and early frost (crystal) growth, or they require several empirically determined constants. The information required by these more complex models is difficult to obtain and may not be available. Eq. (10) requires one empirical constant, β. Using the value of β determined using the experiments presented in this paper, it was possible to predict all the baseline channel flow results and those of other investigators to within the experimental uncertainty. Furthermore, by comparing β for cases with differing flows (with and without vortex generators) it was possible to quantify the effect of vortices on frost growth. Comparisons to other work and the delta-wing data suggest that the model could be modified to account for markedly different Reynolds numbers or flow conditions by selecting a value for β tailored to the particular flow conditions.

The analysis and the experimental data show that Reynolds number and location within the channel have very little influence on frost thickness over the experimental range reported for the baseline channel flow. A delta-wing vortex generator on the channel floor produces a complex laminar vortex system that includes horseshoe and tip vortices. Jacobi and Shah [1] suggested that a horseshoe vortex system would form for this arrangement; however, they note that numerical work reported in the literature did not predict this complex vortex system. The experiments described in the current paper prove the formation of the horseshoe vortex system, and they appear to be the first describing the interaction of the tip vortices and horseshoe vortices generated by this heat-transfer enhancement technique. In the downwash region induced by the streamwise vortices, the frost layer appears more amorphous and less crystalline than in regions influenced by the upwash. Differences in frost structure may be related to the increased frost growth rate observed in the downwash region during mature frost growth. Frost growth with streamwise vortices exhibited a value of β that was about 15% higher than the baseline channel flow; this result indicates that for the same growth period the frost will grow about 7% faster when vortices are present in the channel flow. Although the frost growth rate is slightly higher under vortex-enhanced conditions, the increased growth is much less than the Nusselt number enhancement reported by others. Therefore, the use of vortex generators in refrigeration applications appears promising. Further work to clarify the heat transfer enhancement and pressure-drop penalties of vortex generation refrigerator evaporators is recommended.

Acknowledgements

This research was supported by the Air Conditioning and Refrigeration Center (ACRC). The ACRC is a National Science Foundation, industry, and university cooperative research center at the University of Illinois. The first author also received partial support through an ASHRAE grant-in-aid.

References

[1] A.M. Jacobi, R.K. Shah, Heat transfer surface enhancement through the use of longitudinal vortices: a review of recent progress, Experimental Thermal and Fluid Science 11 (1995) 295–309.

[2] M. Fiebig, Vortex generators for compact heat exchangers, Journal of Enhanced Heat Transfer 2 (1995) 43–61.

[3] F.J. Edwards, C.J.R. Alker, The improvement of forced convection surface heat transfer using surface protrusions in the form of (A) cubes and (B) vortex generators, Proceedings of the Fifth International Heat Transfer Conference, Tokyo 2 (1974) 244–248.

[4] K. Katoaka, H. Doi, T. Komai, Heat/mass transfer in Taylor vortex flow with constant axial flow rates, International Journal of Heat and Mass Transfer 20 (1977) 57–63.

[5] M. Fiebig, P. Kallweit, N. Mitra, S. Tiggelbeck, Heat transfer enhancement and drag by longitudinal vortex generators in channel flow, Experimental Thermal and Fluid Science 4 (1991) 103–114.

[6] S. Tigglebeck, N. Mitra, M. Fiebig, Flow structure and heat transfer in a channel with multiple longitudinal vortex generators, Experimental Thermal and Fluid Science 5 (1992) 425–436.

[7] G. Biswas, H. Chattopadhyay, Heat transfer in a channel with built-in wing-type vortex generators, International Journal of Heat and Mass Transfer 35 (1992) 803–814.

[8] M.C. Gentry, A.M. Jacobi, Heat transfer enhancement by delta-wing vortex generators on a flat plate: vortex interactions with the boundary layer, Experimental Thermal and Fluid Science 14 (1997) 231–242.

[9] W.D. Coles, Experimental determination of thermal conductivity of low density ice, NACA Tech. Note, Paper No. 3143, 1954.

[10] J.D. Yonko, C.F. Sepsy, An investigation of the thermal conductivity of frost while forming on a flat horizontal plate, ASHRAE Transactions 73 (2) (1967) I.1.1–11.

[11] P.L.T. Brian, R.C. Reid, Y.T. Shah, Frost deposition on cold surfaces, Industrial and Engineering Chemistry Fundamentals 9 (1970) 375–380.
[12] P.L.T. Brian, R.C. Reid, I. Brazinsky, Cryogenic frost properties, Cryogenic Technology 5 (1969) 205–212.
[13] G. Biguria, L.A. Wenzel, Measurement and correlation of water frost thermal conductivity and density, Industrial and Engineering Chemistry Fundamentals 9 (1970) 129–138.
[14] N. Yamakawa, N. Takahashi, S. Ohtani, Forced convection heat and mass transfer under frost condition, Heat Transfer—Japanese Research 1 (2) (1972) 1–10.
[15] Y. Hayashi, A. Aoki, S. Adachi, K. Hori, Study of frost properties correlating with frost formation types, Journal of Heat Transfer 99 (1977) 239–245.
[16] W. Woodside, Calculation of thermal conductivity of porous media, Canadian Journal of Physics 36 (1958) 815–823.
[17] H.W. Schneider, Equation of the growth rate of frost forming on cooled surfaces, International Journal of Heat and Mass Transfer 21 (1978) 1019–1024.
[18] Y.X. Tao, R.W. Besant, K.S. Rezkallah, A mathematical model for predicting the densification and growth of frost on a flat plate, International Journal of Heat and Mass Transfer 36 (1993) 353–363.
[19] T.Y. Bong, N.E. Wijeysundera, E.L. Saw, K.O. Lau, Comparison of beta-ray and gamma-ray transmission methods for measurement of frost density distribution, Experimental Thermal and Fluid Science 4 (1991) 567–576.
[20] Y. Mao, R.W. Besant, K.S. Rezkallah, Measurement and correlations of frost properties with airflow over a flat plate, ASHRAE Transactions 98 (2) (1992) 65–78.
[21] A.Z. Sahin, An analytical study of frost nucleation and growth during the crystal growth period, Heat and Mass Transfer 30 (1995) 321–330.
[22] A.Z. Sahin, An experimental study on the initiation and growth of frost formation on a horizontal plate, Experimental Heat Transfer 7 (1994) 101–119.
[23] M.A. Davis, Evaporator calorimeter: the study of overall heat transfer performance, M.S. thesis, University of Illinois at Urbana-Champaign, 1996.
[24] B.D. Storey, Channel frost growth in laminar flows with streamwise vortices, M.S. thesis, University of Illinois at Urbana-Champaign, 1997.
[25] Y. Hayashi, K. Aoki, H. Yuhura, Study of frost formation based on a theoretical model of the frost layer, Transactions of the Japan Society of Mechanical Engineers 40 (1976) 885–899.
[26] J.G. Georgiadis, P. Greywall, A. Tenbusch, Visualization of hoar frost with confocal microscopy, International Mechanical Engineering Congress and Exposition, Transport Phenomena in Solidification, 171–175, Chicago, 1994.
[27] N. Fukota, Experimental studies in the growth of small ice crystals, Journal of Atmospheric Science 26 (1969) 522–531.
[28] Y. Mao, The measurement and analysis of frost accumulation on a flat plate in forced convection, M.S. thesis, University of Saskatchewan, 1991.
[29] M.C. Gentry, Heat transfer enhancement using tip and junction vortices, PhD thesis, University of Illinois at Urbana-Champaign, 1998.